



RESEARCH ARTICLE SUMMARY

NEUROSCIENCE

A petavoxel fragment of human cerebral cortex reconstructed at nanoscale resolution

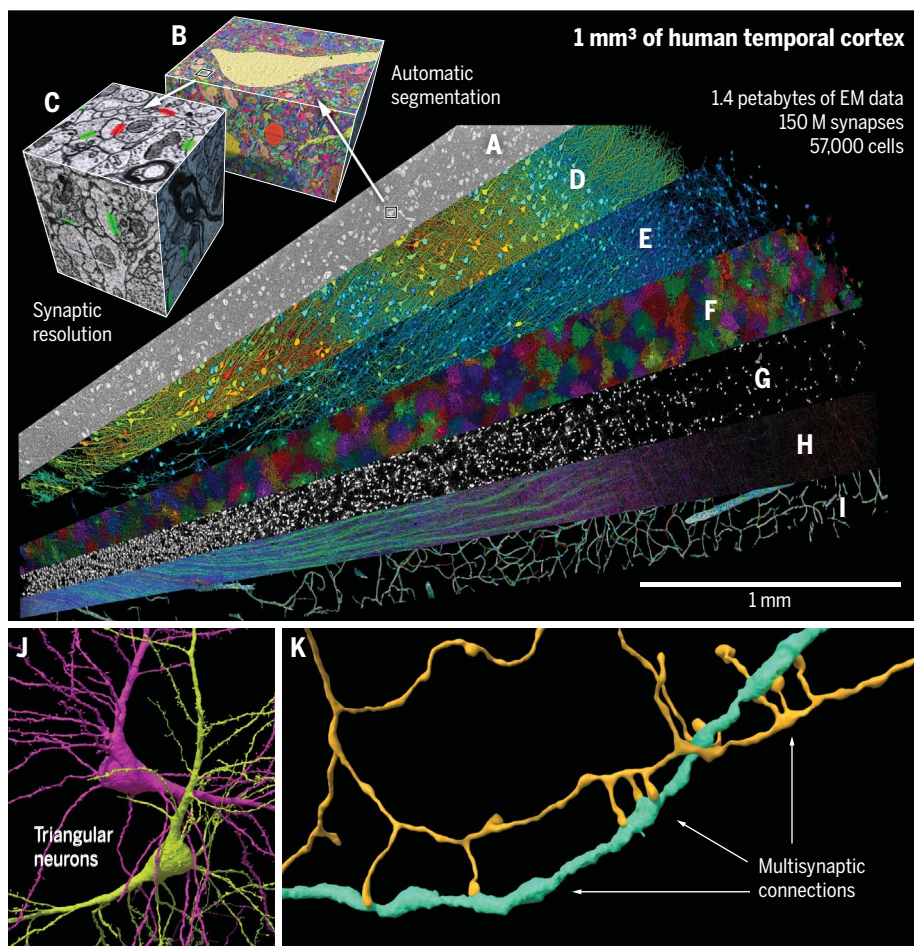
Alexander Shapson-Coe[†], Michał Januszewski[†], Daniel R. Berger[†], Art Pope, Yuelong Wu, Tim Blakely, Richard L. Schalek, Peter H. Li, Shuhong Wang, Jeremy Maitin-Shepard, Neha Karlupia, Sven Dorkenwald, Evelina Sjostedt, Laramie Leavitt, Dongil Lee, Jakob Troidl, Forrest Collman, Luke Bailey, Angerica Fitzmaurice, Rohin Kar, Benjamin Field, Hank Wu, Julian Wagner-Carena, David Aley, Joanna Lau, Zudi Lin, Donglai Wei, Hanspeter Pfister, Adi Peleg, Viren Jain*, Jeff W. Lichtman*

INTRODUCTION: Although the functions performed by most of the vital organs in humans are not very different compared with other animals, those performed by the human brain clearly separate us from the rest of life on the planet. However, detailed knowledge concerning the synaptic circuitry underlying human brain function is lacking. Connectomic

imaging approaches are now available to render neural circuits of sufficiently large volume and high enough resolution to study the connectivity at the level of individual neurons and their synaptic connections but over a scale comprising thousands of neurons. Generating such a dataset was the goal of this project.

RATIONALE: One critical barrier to obtaining high-quality human brain tissue. Organ biopsies provide valuable information in many human organ systems, but biopsies are rarely done in the brain except to examine or excise neoplastic masses, so most of them are problematic for the investigation of normal human brain structure. One attempt has been to use brain organoids made from human cells, but at present, they do not approximate brain tissue architectonics (e.g., cortical layers are not present). A direct approach would be to map cells and circuits from human specimens made available from neurosurgical interventions for neurological conditions in which pieces of the cortex are discarded because they obstruct access to a pathological site. We posited that the human brain tissue that is a by-product of neurosurgical procedures could be leveraged to study normal—and ultimately disordered—human neural circuits.

Downloaded from https://www.science.org at Harvard University on October 01, 2024



The shared H01 dataset. A range of histological features in 1 mm³ of human brain were rendered, including neuropil (A) and its segmentation (B) at nanometer resolution, annotated synapses (C), excitatory neurons (D), inhibitory neurons (E), astrocytes (F), oligodendrocytes (G), myelin (H), and blood vessels (I). A previously unrecognized neuronal class (J) and multisynaptic connections (K) were also identified.

RESULTS: Here, we describe such a sample of human temporal cortex, 1 mm³ in volume, which extends through all cortical layers. The sample was obtained during surgery to gain access to an underlying hippocampal lesion from a patient with epilepsy. We imaged this sample by high-throughput serial section electron microscopy, generating a petascale dataset that was analyzed with new tools and computationally intensive methods. We reconstructed thousands of neurons, more than a hundred million synaptic connections, and all of the other tissue elements that comprise human brain matter, including glial cells, the blood vasculature, and myelin. Because the dataset is large and incompletely scrutinized, we are sharing all of the data in an online resource (<https://h01-release.storage.googleapis.com/landing.html>) and also providing tools for analysis and proofreading. We found a previously unrecognized class of directionally oriented neurons in deep layers (see figure, panel J) and very powerful and rare multisynaptic connections between neurons throughout the sample (see figure, panel K).

CONCLUSION: This work provides evidence of the feasibility of human connectomic approaches to visualize and ultimately gain insight into the physical underpinnings of normal and disordered human brain function. It is hoped that this endeavor will be aided by providing free access to all of the data and relevant tools. ■

The list of author affiliations is available in the full article online.

*Corresponding author. Email: jeff@mcb.harvard.edu (J.W.L.); viren@google.com (V.J.)

†These authors contributed equally to this work.

Cite this article as Shapson-Coe et al., *Science* 384, eadk4858 (2024). DOI: 10.1126/science.adk4858

S **READ THE FULL ARTICLE AT**
<https://doi.org/10.1126/science.adk4858>

RESEARCH ARTICLE

NEUROSCIENCE

A petavoxel fragment of human cerebral cortex reconstructed at nanoscale resolution

Alexander Shapson-Coe^{1,2†}, Michał Januszewski^{3†}, Daniel R. Berger^{1†}, Art Pope⁴, Yuelong Wu¹, Tim Blakely⁵, Richard L. Schalek¹, Peter H. Li⁴, Shuhong Wang¹, Jeremy Maitin-Shepard⁴, Neha Karlupia¹, Sven Dorkenwald^{4,6,7}, Evelina Sjostedt¹, Laramie Leavitt⁴, Dongil Lee^{1,8}, Jakob Troidl⁹, Forrest Collman¹⁰, Luke Bailey¹, Angerica Fitzmaurice^{1,11}, Rohin Kar^{1,11}, Benjamin Field^{1,11}, Hank Wu^{1,11}, Julian Wagner-Carena¹, David Aley¹, Joanna Lau¹, Zudi Lin⁹, Donglai Wei¹², Hanspeter Pfister⁹, Adi Peleg^{1,13}, Viren Jain^{4*}, Jeff W. Lichtman^{1*}

To fully understand how the human brain works, knowledge of its structure at high resolution is needed. Presented here is a computationally intensive reconstruction of the ultrastructure of a cubic millimeter of human temporal cortex that was surgically removed to gain access to an underlying epileptic focus. It contains about 57,000 cells, about 230 millimeters of blood vessels, and about 150 million synapses and comprises 1.4 petabytes. Our analysis showed that glia outnumber neurons 2:1, oligodendrocytes were the most common cell, deep layer excitatory neurons could be classified on the basis of dendritic orientation, and among thousands of weak connections to each neuron, there exist rare powerful axonal inputs of up to 50 synapses. Further studies using this resource may bring valuable insights into the mysteries of the human brain.

The human brain is a vastly complicated tissue and, to date, little is known about its cellular microstructure, including the synaptic circuits. Disruption of these circuits is likely associated with various brain disorders. Technologies such as diffusion magnetic resonance imaging (MRI) tract tracing (1), high-resolution MRI (2), functional MRI (fMRI) (3), and others [see reviews in (4, 5)] have improved our knowledge of the structure and function of the human brain at and below millimeter resolution. However, to identify the structure of neural networks at the synaptic level requires orders of magnitude higher resolution using light microscopy or electron microscopy (EM). Light microscopy approaches to visualizing neural networks have been successful in tracing full connectivity in the peripheral nervous system, where the density of axons is relatively low compared with the central nervous system (6, 7). Light-based

methods in the central nervous system are advancing rapidly (8–16), but for dense neural networks, the most successful approaches in the brain have used volume EM, in which reconstruction of every cellular element and synapse is possible due to the extremely high spatial resolution afforded by the short wavelength of electrons (17–25). Because of automation and rapid imaging modalities, serial EM can now scale to image cubic millimeter volumes at nanometer resolution. Here, we used these approaches in a human brain tissue sample.

High-quality human brain tissue specimens are available from neurosurgical interventions in living individuals in whom part of the cortex was removed because it obstructed access to a pathological region. Here, we describe such a sample, a rapidly preserved (see the materials and methods), 170-μm-thick slab of human cortex from the anterior part of the middle temporal gyrus of a 45-year-old female. The sample has a total volume of just over 1 mm³ and was removed to gain access to an epileptic focus in the underlying hippocampus. An important caveat related to human surgical samples is that they originate in individuals with pathologies of the nervous system such as epilepsy, tumors, or neurodegenerative diseases. In this case, we cannot exclude the possibility that long-term epilepsy, or its pharmacological treatment, had subtle effects on the nanometer-scale structure of the sample. However, at least by light microscopy-based neuropathological examination, the sample was deemed normal, lacking, e.g., the band of aggregated neurons that is seen in the outer part of layer 2 when

hippocampal sclerosis associated with epilepsy extends into the adjacent temporal lobe (26).

We sought to reconstruct a human sample spanning all six layers of cortex, which is ~3 mm from layer 1 to the white matter. The throughput limits of serial section EM constrained the total thickness of the reconstructed sample. However, because the sample is oriented perpendicular to the pia and follows the fanned-out directions of the principal axons and dendrites of pyramidal neurons, many of these could be traced across cortical layers. The acquisition, computational alignment, automated three-dimensional (3D) segmentation, and automated synaptic annotation of digital human brain tissue at this large scale and fine resolution not only enables access to neuronal circuitry comprising thousands of neurons and millions of synapses, but also provides a clear view of all the other tissue elements that comprise human brain matter, including the glial cells and blood vasculature, and of the relationships between various cell types. A wide range of questions related to human brain biology are thus open to scrutiny from a single sample, which we have named H01. To aid in its analysis, we are sharing all of the data from H01 and the tools used to analyze it in an online resource: <https://h01-release.storage.googleapis.com/landing.html>.

The reconstructed brain sample

The sample that we analyzed is from the left anterior middle temporal gyrus resected to gain access to an underlying epileptic focus. It was subjected to rapid fixation, stained with heavy metals (27) and embedded in resin, after which 5019 sections with a mean thickness of 33.9 nm were collected on tape (28), giving a total thickness of 170 μm (see the materials and methods). Each section was imaged by multibeam scanning EM at 4 × 4 nm² resolution (Fig. 1A and table S1) and aligned (Fig. 1B), yielding a dataset ~1.4 petabytes in size and 1.05 mm³ in volume after correcting for sectioning-induced tissue compression (see the materials and methods).

We generated a 3D reconstruction of nearly every cell and process in the aligned volume using a multiresolution flood-filling network (FFN) (29). This produced fragments of whole objects (base segments), which were then agglomerated to produce larger objects, including cell bodies with axons and dendrites (Fig. 2, A and B; see the materials and methods). However, this process of agglomeration gave rise to merge errors between nearby objects, such as a passing axon and dendrite, which in many cases could be corrected using automatic classification of the objects (Fig. 2C; see the materials and methods). Because there was a trade-off between removing split errors and adding merge errors, we generated two different agglomerations in the online platform

¹Department of Molecular and Cellular Biology, Center for Brain Science, Harvard University, Cambridge, MA 02138, USA.

²Queen Mary, University of London, London E1 4NS, UK.

³Google Research, Zürich 8002, Switzerland. ⁴Google Research, Mountain View, CA 94043, USA. ⁵Google Research, Seattle, WA 98103, USA. ⁶Princeton Neuroscience Institute, Princeton University, Princeton, NJ 08540, USA. ⁷Computer Science Department, Princeton University, Princeton, NJ 08540, USA.

⁸Department of Bio and Brain Engineering, Korea Advanced Institute of Science and Technology, Daejeon 34141, Republic of Korea. ⁹School of Engineering and Applied Sciences, Harvard University, Cambridge, MA 02138, USA. ¹⁰Allen Institute for Brain Science, Seattle, WA 98109, USA. ¹¹Northeastern University, Boston, MA 02115, USA. ¹²Computer Science Department, Boston College, Chestnut Hill, MA 02467, USA.

¹³Google, Cambridge, MA 02142, USA.

*Corresponding author. Email: jeff@mcb.harvard.edu (J.W.L.); viren@google.com (V.J.).
†These authors contributed equally to this work.

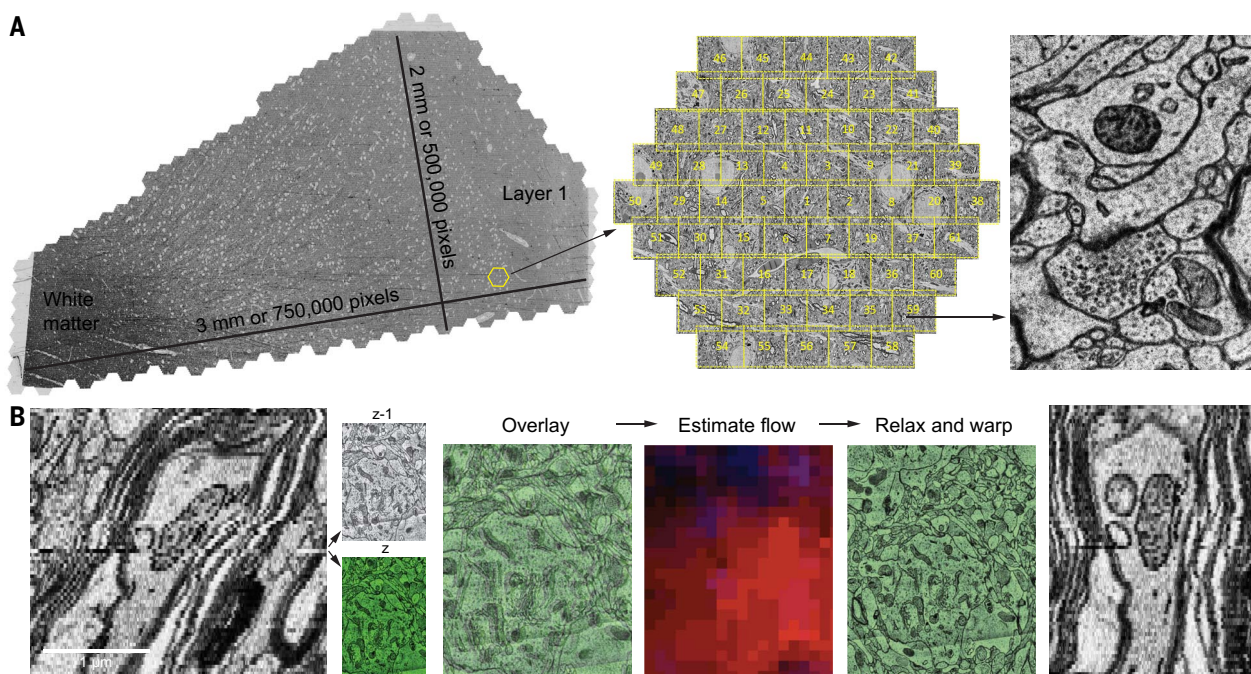


Fig. 1. H01 dataset, image acquisition, and alignment. (A) A fresh human surgical cerebral cortex sample was rapidly preserved, stained, embedded in resin, sectioned at ~33 nm, collected on tape, and imaged using the ATUM-multibeam SEM (ATUM-mSEM) method. The Zeiss mSEM electron microscope uses 61 beams that image a hexagonal area of ~10,000 μm^2 simultaneously, which allows for large areas to be imaged rapidly. For each section, all of the resulting tiles were then stitched together (left); this section is ~4.5 mm^2 in area and was imaged with $4 \times 4 \text{ nm}^2$ pixels. Image of synapse is shown at right. Given the necessity of some overlap between the stitched tiles, this single

section required the collection of >300 gigabytes of data. (B) Fine-scale alignment with optical flow. Left: an x-y cross-section of the initial coarsely aligned subvolume exhibits drift and jitter. Center: two adjacent XY sections, z (green) and z-1, are overlaid to illustrate their misalignment. Image patch-based cross-correlation computes an x-y flow field between them. Red and blue intensities, which indicate the respective horizontal and vertical flow components, were used to warp one of the sections, improving their alignment (relax and warp overlay). Right: x-z view of the same subvolume with flow realignment applied.

Neuroglancer (https://h01-dot-neuroglancer-demo.appspot.com/#!gs://h01-release/assets/neuroglancer_states/20230907/c2_vs_c3.json). The c2 agglomeration favored fewer split errors (and thus longer processes) but with a higher number of merge errors. Conversely, the c3 agglomeration had more split errors but fewer merge errors. By proofreading neurons in Neuroglancer (https://h01-dot-neuroglancer-demo.appspot.com/#!gs://h01-release/assets/neuroglancer_states/20230907/proofread_cells.json; see table S2 and the materials and methods), we found that the c3 agglomeration required 1.6-fold less correction of merge errors (257 versus 400 merge correction operations per cell, $P < 10^{-7}$, $n = 104$, Student's paired t test) but 2.1-fold more correction of split errors (504 versus 238 split correction operations per cell, $P < 10^{-10}$, $n = 104$, Student's paired t test) when compared with the c2 agglomeration (excluding dendritic spines). Split errors were not uniformly distributed across the H01 volume (fig. S1; see the materials and methods), as shown by mapping the tendency (blue: high, red: low) of segments in the c3 agglomeration to traverse consecutive z layers in Neuroglancer (https://h01-dot-neuroglancer-demo.appspot.com/#!gs://h01-release/assets/neuroglancer_states/20230907/c2_vs_c3.json).

[h01-release/assets/neuroglancer_states/20230907/unique_segment_density_plot_h01.json](https://h01-dot-neuroglancer-demo.appspot.com/#!gs://h01-release/assets/neuroglancer_states/20230907/unique_segment_density_plot_h01.json)). Merge errors in the base segmentation itself were rare, being observed in only 13 of 365,404 base segments comprising the proofread neurons (0.0036%). All subsequent analyses in the present study were based on the c3 agglomeration.

Synapse prediction

Identifying synapses was necessary to analyze the connectivity between neurons in this dataset. As shown in Fig. 2D, we used machine learning tools to train automated synapse classifiers to identify the pre- and postsynaptic component of each synapse and determine whether the presynaptic terminal was excitatory or inhibitory (see the materials and methods). Manual proofreading of a selection of axons covering all cortical layers showed that the number of missed synapses (false negatives) for excitatory and inhibitory synapses was 11 and 35%, respectively. The false discovery rate for excitatory and inhibitory synapses was 3.2 and 2.7%, respectively (table S3). In total, 149,871,669 synapses were automatically detected in the volume. A total of 111,272,315 synapses were classified as excitatory and 38,599,354 as inhibitory. Based on proofreading, excitatory and inhibitory

synapses were classified correctly 86.89 and 84.98% of the time, respectively. Adjusting for the measured false discovery, false-negative, and excitatory or inhibitory misclassification rates, we estimate that the H01 volume contains a total of 102.5 million (67.1%) excitatory synapses and 50.3 million (32.9%) inhibitory synapses. Analyzing the postsynaptic component of 133,704,881 of the automatically identified synapses (see the materials and methods), we found, as expected, a high percentage of these synapses located on dendrites (99.4%), with far fewer innervating the axon initial segments (AIS, 0.197%) or somata (0.394%).

Tools for cell reconstruction and circuit exploration

Although some analyses of the data will not be affected by the agglomeration split and merge errors described above, other analyses, particularly those at the level of neuronal circuits, require correction of these agglomeration errors by proofreading. Because of the large number of neuronal structures, it is infeasible for a single laboratory to proofread the entire dataset manually. To facilitate scientific studies that require correction of agglomeration errors

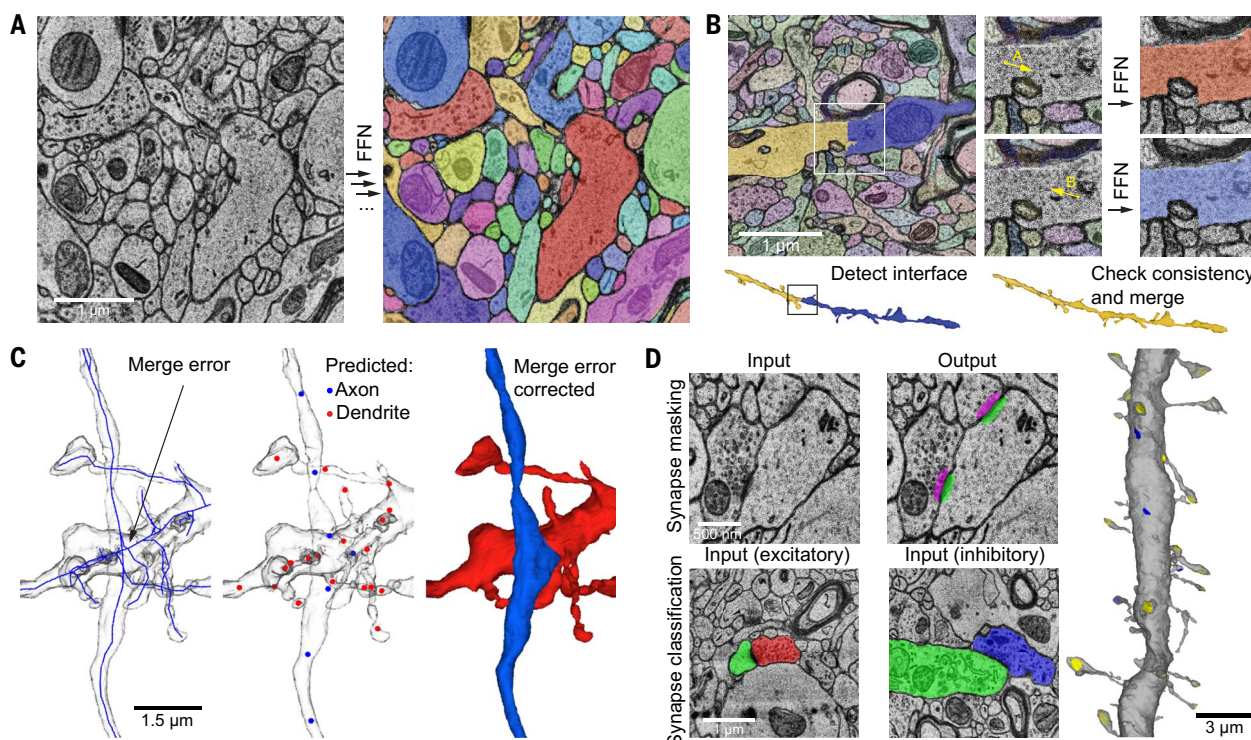


Fig. 2. Segmentation, split correction, and merge error correction through neuronal subcompartment classification and synapse prediction. (A) Example of sequential segmentation with an FFN. Objects are filled sequentially from seed locations until the 3D volume is segmented completely. (B) FFN agglomeration. Left: site between two adjacent base segments (white box is the 2D image; black box below shows the 3D image) is a candidate agglomeration location. Center: FFN segmentation is seeded from points A and B independently. Right: If the resulting A and B segmentations are mutually consistent, then the object pair is merged (below). (C) Subcompartment prediction and merge error correction. Left: a single reconstructed object with a merge error where axon and dendrite cross near each other. The object is converted to a reduced skeleton representation (blue). Middle: fields of view around a subset of skeleton nodes are input to a subcompartment classification model. Red nodes show a predicted dendrite; blue nodes show a predicted axon. The inconsistency in subcompartment predictions is detected, and

the agglomeration graph is cut at the location that maximally improves subcompartment consistency. Right: the separated axon and dendrite after applying the suggested cut; a 3D rendering of separated fragments with subcompartment predictions can be seen in Neuroglancer (https://h01-dot-neuroglancer-demo.appspot.com/#!gs://h01-release/assets/neuroglancer_states/20240424/fig2c.json). (D) Synapse detection and classification. Top: x-y cross-section of EM image input to synapse detection model (left) and the resulting presynaptic (magenta) and postsynaptic (green) prediction masks (right). Bottom: cross-section of EM image and presynaptic (left red, right blue) and postsynaptic (green) object segmentation inputs to excitatory versus inhibitory classification model. Right: 3D rendering of a dendrite with predicted incoming excitatory (yellow) and inhibitory (blue) synaptic sites; a 3D rendering of all inputs to this neuron can be seen in Neuroglancer (https://h01-dot-neuroglancer-demo.appspot.com/#!gs://h01-release/assets/neuroglancer_states/20210601/figs/fig2d.json).

by proofreading, we provide a collaborative online proofreading platform for H01 (<https://h01-release.storage.googleapis.com/proofreading.html>), which is built upon the CAVE (Connectome Annotation and Versioning Engine) infrastructure (30). This tool is web based and tightly integrated with the Neuroglancer viewer. Proofreaders can interactively update the segmentation by correcting merge and split errors. All proofreaders have access to the most up-to-date segmentation at all times to avoid redundant edits by multiple community members. We selected the c3 agglomeration as a starting point for the collaborative proofreading process. Anyone can apply to become a proofreader, and proofreaders may download data relating to the cells that they have proofread for subsequent analyses, as demonstrated in online tutorials (<https://github.com/VCG/cave-scripts>). The most recent version of the

proofread volume is always available to browse in Neuroglancer (https://ngl.brain-wire.org/#!gs://h01-release/assets/neuroglancer_states/cave/demo.json) by any interested researcher without applying to be a proofreader.

VAST (Volume Annotation and Segmentation Tool) (31) is a versatile, free software tool (<https://lichtman.rc.fas.harvard.edu/vast/>) that can be used to view, segment, and annotate large voxel datasets. In contrast to the CAVE system described above, which focuses mainly on the correction of split and merge errors of the agglomerated segmentation, VAST can be used to generate new ground-truth segmentations of objects of interest (e.g., vasculature or organelles) by manual voxel painting and to create annotated binary skeletons for quantitative analysis (e.g., volume or length measurements). VAST can also be used to agglomerate c2 or c3 segments locally. To make the H01 image

data available in VAST, we extended the program to read data directly from the Neuroglancer-compatible online storage. Results from VAST can be exported in various formats for analysis and visualization. VAST also includes an application programming interface (API) that allows for script-based automation using Matlab. VAST was used for several results in this study, including the manual labeling and classification of all cell bodies described below.

For analysis, various databases are available in the H01 online resource (<https://h01-release.storage.googleapis.com/data.html>) to enable specific queries about the cellular and synaptic data. However, these are not integrated with the Neuroglancer platform and they do not support more complex queries at the neuronal network level. To address this, we developed a stand-alone program, CREST (Connectome Reconstruction and Exploration Simple Tool). CREST

can be used to identify and explore the connections of cells based on a number of those cells' features, including the numbers of synaptic inputs or outputs of a given strength (see strong synaptic connections described below). CREST can also be used to explore and graph chains of synaptically connected neurons, finding both how a neuron's postsynaptic influence diverges across multiple generations of downstream neurons and how presynaptic influences converge from multiple generations of upstream neurons. It should be noted that paths identified in this way require manual verification given the presence of agglomeration merge errors and, to a lesser extent, synapse false positives. Verified paths of interest can be saved locally, along with the schematic view of the path, for later re-viewing using the CREST tool. Finally, CREST also features a proofreading tool that allows cells to be proofread and each version of a cell saved locally. Detailed user instructions and the CREST program are available from the CREST home page (<https://github.com/ashapsoncoe/CREST>).

Cellular and synaptic organization

The entire segmented volume (Fig. 3), including the synaptic and subcompartment annotations, are available for exploration within the Neuroglancer platform. A video demonstration of how to explore the various data overlays, modify their appearance, and navigate the H01 dataset is available online (32).

The H01 resource is divisible into many subcategories. On the basis of skeleton node classifications and manual annotations, and excluding extracellular spaces, myelinated axon sheaths, and tissue artifacts (see the materials and methods), the neuropil by volume is composed of unmyelinated axons (~40.2%), dendrites (~25.8%), glial processes (~15.5%), somata (~9.4%), myelinated axons excluding their sheaths (~7.5%), collapsed blood vessels (~1.5%), AIS (~0.07%), and cilia (~0.03%) (see

also table S4 for breakdown by cortical layer). In addition to these well-known categories, we found a number of unidentified cortical objects that accounted for very little volume (fig. S2).

We analyzed all of the cells with nuclei in the sample (Fig. 4), manually identifying and quantifying them (table S5, table S6). There were 49,080 neurons and glia (Fig. 4A) and 8100 blood vessel-related cells (57,180 cells total; Fig. 4B). Glia outnumbered neurons 2:1 (32,315 versus 16,087). Of the neurons, 65.5% were spiny (10,531, of which 8803 had a pyramidal shape), 29.1% were nonspiny and nonpyramidal and thus classified as interneurons (4688), and 5.4% (868) did not easily fit into this binary categorization mostly because their somata were not fully in the volume. There were also some unusual neurons that were difficult to classify; examples of this last category are shown in fig. S3. Overall, the density of neurons was \sim 16,000/mm³, approximately one-third lower than previously estimated from light microscopy of human temporal cortex (33) and nearly 10-fold lower than the density of the association cortex of the mouse (34–36).

The cells within the sample showed macroscopic organization: Cortical layers were clearly distinguishable by cell soma volume (Fig. 4A). To find an objective layering boundary criterion, we used cell soma size and clustering density, generating a six-layered cortex and white matter (fig. S4; see the materials and methods). The fiducial lines in each panel of Fig. 4 are based on these layers (named in Fig. 4A). There were fewer cells with large cell bodies in the white matter and cortical layer 1 because these regions were populated mainly by glial cells with cell body sizes that were smaller than neurons (Fig. 4A, blue). The largest cells (Fig. 4A, red) were mostly in a broad, deep, infragranular band corresponding to layer 5 and a supragranular band corresponding to layer 3, as expected (37). The 3D shape of cells plus their EM appearances allowed their classification into types.

The largest cell somata belonged to spiny pyramidal neurons, with variation in soma size across the cortical layers (Fig. 4C). Nonpyramidal neurons were much less spiny, had smaller cell body sizes, and as a group were not obviously arranged into layers (Fig. 4D).

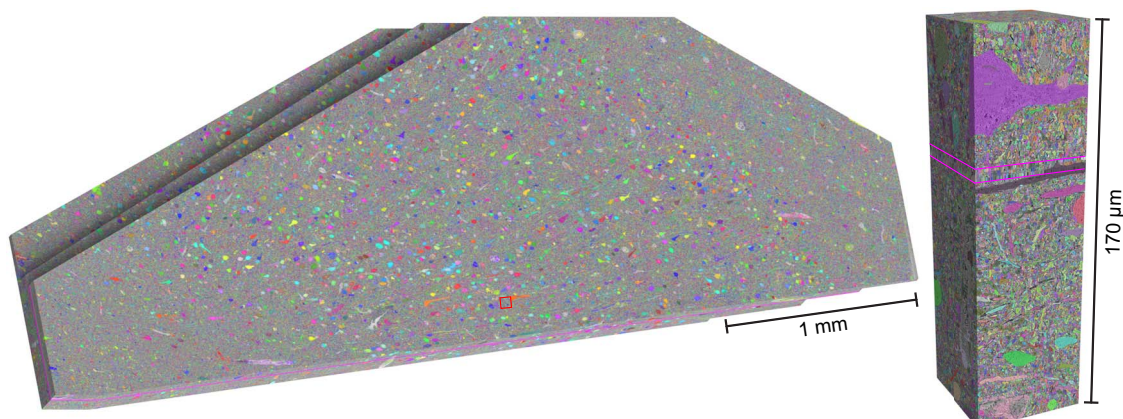
The glial cells did show differences between the layers (Fig. 4, E to G). The compact and complicated arbors of protoplasmic astrocytes were densely tiled in layers 2 to 6, as described previously (38–40). However, in the more superficial parts of layer 1, they were often more intermingled, had a higher density, and were smaller in size (Fig. 4E and fig. S5, A, B, and E). Fibrous astrocytes in the white matter were more elongated than those that occupied the cortical layers.

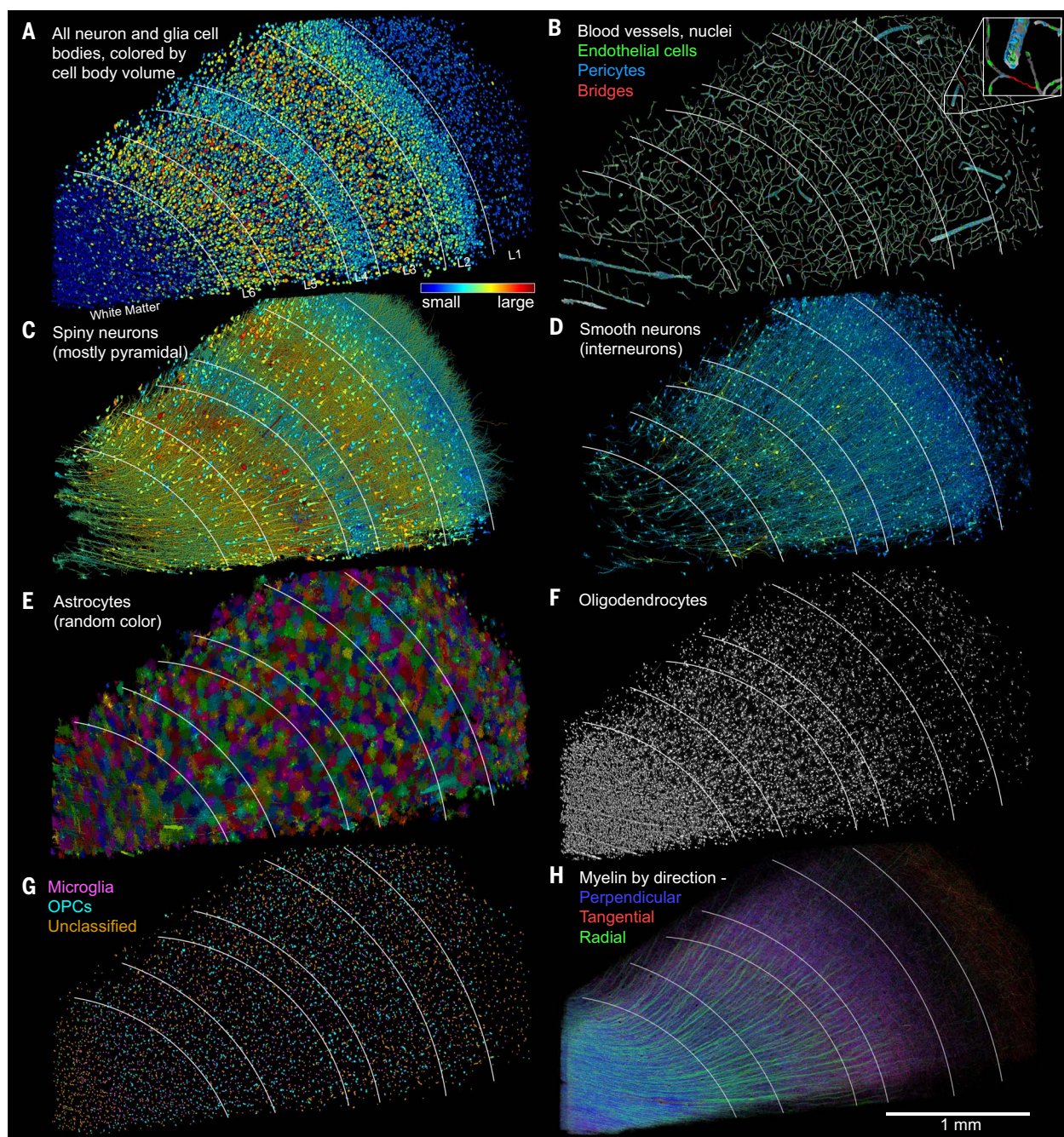
Two other kinds of glia, microglia and oligodendrocyte precursor cells (OPCs), had almost even density across all layers but showed affinity for the vasculature (fig. S5C), whereas astrocyte cell bodies did not (41). Because of the similar morphologies of OPCs and microglia, a self-supervised machine learning approach (SegCLR) was used to distinguish these types [see the materials and methods and (42)], with 2517 cells predicted to be microglia, 1626 predicted to be OPCs, and 2102 that were unclassified (Fig. 4G and fig. S6).

Another type of glia, oligodendrocytes ($n = 20,139$), were distributed according to a gradient, with the lowest density in the upper layers and highest density in the white matter, as would be expected given their role in myelin formation (Fig. 4F and fig. S5E). Like microglia and OPCs, oligodendrocytes showed affinity for blood vessels (fig. S5C). Perivascular oligodendrocytes formed lines along radially oriented blood vessels in the white matter and to a lesser degree elsewhere in the volume (fig. S5D). Myelin, a product of oligodendrocytes, followed the oligodendrocyte density gradient, with the highest density in the white matter and the lowest in layer 2 (Fig. 4H and table S4). A

Fig. 3. Segmented H01

volume. Left: oblique view of the H01 dataset after all automatic segmentation steps, which has been trimmed to the fully imaged volume and stretched to compensate for section compression from ultrathin sectioning. The C3 auto-segmentation is overlaid in random colors. Right: cut-out of the dataset at the location of the red rectangle showing a cross-section of the aligned image stack. The pink lines show where the two sectioning series join (phase 1 and phase 2).





Downloaded from https://www.science.org at Harvard University on October 01, 2024

Fig. 4. Distribution of cells, blood vessels, and myelin in the sample. White lines indicate layer boundaries based on cell clustering. (A) All 49,080 cell bodies of neurons and glia in the sample colored by soma volume. (B) Blood vessels and the nuclei of the 8136 associated cells; 3D renderings of all blood vessels can be viewed in Neuroglancer (https://h01-dot-neuroglancer-demo.appspot.com/#/gs://h01-release/assets/neuroglancer_states/20240424/fig4b.json). Inset shows a magnified view of the location of the individual cell types. (C) Spiny

neurons ($n = 10531$; putatively excitatory) colored by soma volume. (D) Interneurons ($n = 4688$; few spines, putatively inhibitory) colored by soma volume. (E) Astrocytes ($n = 5474$). (F) Most of the oligodendrocytes ($n = 20139$) in the volume. (G) Cell bodies ($n = 6702$) of microglia and OPCs. (H) Myelinated axons in the volume color coded by topological orientation. Most axons in white matter run in the perpendicular direction. Images and scale bar are without correction for ultrathin sectioning compression.

substantial number of myelinated axons ran radially between the white matter and superficial layers (Fig. 4H, green) and horizontally within layers in two orthogonal axes (Fig. 4H, red and blue). In layer 1, a set of large-caliber myelinated axons ran tangentially through

our slice parallel to the pia. The myelin in the white matter ran primarily orthogonal to the plane of the section (Fig. 4H, blue) and (Fig. S7). These axon orientations can be used to validate diffusion tensor imaging signals in the human brain *in vivo* (43, 44).

The reconstructed blood vessels (~230 mm in length) did not show much evidence of layer-specific behavior but had a lower density in the regions surrounding large vessels and in the white matter (Fig. 4B), presumably because of the lower metabolic demands of myelinated

axons for ATP to maintain transmembrane ionic gradients (45). The vasculature was lined by 4604 endothelial cells (Fig. 4B, green, ~20/mm of vasculature) and a more heterogeneous group of 3549 pericytes and other perivascular cell types (Fig. 4B, blue, ~15/mm of vasculature) also within the basement membrane but displaced slightly further from the lumen (Fig. 4B). Bloodless bridges ($n = 74$), composed of basement membrane and pericytes but lacking endothelial cells and a lumen (46–48), connected different capillaries in the dataset (Fig. 4B, red).

From a functional standpoint, a critical component of brain tissue is its synapses. Using a U-Net classifier, ~150 million synapses were identified and divided into two categories, excitatory and inhibitory (see the materials and methods). The density of the ~111 million excitatory synapses was highest in layers 1 and 3 (Fig. 5A), whereas the ~39 million inhibitory synapses peaked in density in layer 1 (Fig. 5B). The percentage of excitatory synapses of total [calculated as excitatory/(excitatory + inhibitory)] was broadly similar across layers, being slightly lower in layer 1 (Fig. 5C), as previously reported (33). The identification of all synapses and their assignment to specific pre- and postsynaptic partners allowed the rendering of excitatory and inhibitory input to each pyramidal cell (Fig. 5D). In the pyramidal neuron shown in Fig. 5D, as in other excitatory neurons, the synapses on the AIS, cell body and proximal dendrites were largely inhibitory (blue), whereas in the spiny dendritic regions, there were more excitatory synapses (orange) than inhibitory ones. Such excitatory and inhibitory compartmentalization was not evident on interneurons (e.g., see Fig. 5E). Comparing the ratio of excitatory to inhibitory input in each cortical layer onto pyramidal neurons and interneurons showed that the excitatory to inhibitory balance varied slightly between layers, with the highest proportion of inhibitory input tending to occur in the layer in which the given cell type's soma resides (Fig. 5F and table S7).

To determine what kinds of biological insights might be made from the use of this resource, we then examined two phenomena that we came across while looking at the image data.

Morphological subcategories of layer 6 triangular neurons

The deepest layer of the cerebral cortex is not as well characterized as more superficial layers (49), in part because it contains a greater diversity of cell types, especially in primates (50). This resource provides a large set of deep layer neurons and can therefore potentially be used to better characterize these cell types. We analyzed the so-called “triangular” or “compass” cells that reside in layer 6 but are not well understood (49, 51–53). These spiny neurons

are characterized by an apical-going dendrite; however, unlike pyramidal neurons, they each have one especially large basal dendrite rather than a more uniform skirt of basal dendrites. We identified all of the triangular neurons in the H01 volume (Fig. 6A), most of which resided in layers 5 and 6 ($n = 876$), comprising approximately one-third of the spiny neurons in these layers.

The large basal dendrites of triangular neurons emerged from the cell somata at various angles (hence the name “compass cell”), ranging from 180° from the apical dendrite (i.e., toward the white matter) to ~90° from the apical dendrite. The mean orientation was ~126° (Fig. 6B). We could group many of these cells into two categories along the anterior-posterior axis: those in which the basal dendrite projected toward section 1 (in the “reverse-going” direction) and those in which the basal dendrite projected in the opposite (“forward-going”) direction, toward section 5292 (green and magenta cells, respectively; Fig. 6, C and D, and movie S1). By taking into account the curvature of the layers, we obtained a locally calculated average apical dendrite direction (i.e., in the “radial direction” toward the pia; see fig. S8). Using these data and the orientation of the basal dendrite, we found that the majority (~77.5%) of the triangular cells were either clearly forward-going ($n = 347$) or reverse-going ($n = 339$), forming a bimodal distribution, whereas the rest had basal dendrites that were more tangential ($n = 186$; four cells were outliers with basal dendrites pointing toward the radial direction) (Fig. 6, E to G). The axis formed by these basal dendrites is the main axis of the myelinated axons in the subjacent white matter, which, based on the information available, is the anterior-posterior axis of the temporal lobe.

The fact that the basal dendrites, on average, pointed slightly toward the white matter meant that the two sets of basal dendrites were not parallel to each other. Rather, each subgroup had basal dendrites at mirror symmetrical angles (Fig. 6, C and D). Moreover, we found other mirror symmetrical features, such as the relative absence of branches on the upper side of the basal dendrite and the scarcity of apical dendrite branches pointing in the same direction as the basal dendrite (see, e.g., Fig. 6D).

When we rendered the two subgroups of neurons (forward-going or reverse-going), it appeared that they were not uniformly distributed. To avoid identification bias at the border of the image stack, we included only neurons with cell bodies located in the middle half of the volume (centered in sections 1323 to 3970; $n = 431$; Fig. 6, H to J). We then analyzed the nearest neighbor triangular cell to each of these neurons and found that its basal dendrite pointed in the same direction as the basal dendrite of its nearest neighbor more often than would be expected by chance, showing statisti-

tically significant clustering (Fig. 6K; Fisher's exact test, $P = 0.005$). This indicates that these cells do cluster to some degree. Patchiness of axonal projections to layer 6 has been seen with anterograde labeling experiments in humans (54). What the function of this bimodal distribution of triangular cell basal dendrite directions signifies remains to be determined.

Multisynaptic connections between axons and specific postsynaptic partners

Previous work showed that axons in rodent cerebral cortex occasionally establish multiple synapses on the same postsynaptic cell (25, 55). We sought to determine whether the same phenomenon exists in human cerebral cortex. CREST was used to systematically identify strong connections (see the materials and methods for details), where a single axon established multiple synapses on the same postsynaptic cell. Many examples of this phenomenon were found. These included excitatory and inhibitory axons that innervated excitatory and inhibitory postsynaptic dendrites in any combination (Fig. 7, A to D). These strong connections were rare. For nearly all cells, the histogram of the number of synapses per axonal input showed a rapid decline from the most common occurrence, where an axon established one synapse with a target cell (96.49%). Two synapse contacts occurred uncommonly (2.99%), even fewer three-synapse contacts were observed (0.35%), and connections with four or more synapses occurred rarely (0.092%; see table S8 for counts of inputs to all neurons). Despite the overall rarity of strong connections, however, we found that 39% of the 2743 neurons that were well innervated in the volume (i.e., having at least 3000 synapses onto their dendrites) had at least one input with seven or more synapses, raising the possibility that rare, powerful axonal inputs are a general characteristic of neuronal innervation in human cerebral cortex. These analyses excluded chandelier cell axons innervating AIS, which are well known to make multisynaptic connections (56). It should also be noted that these results are based on the uncorrected c3 agglomeration data with many axonal splits and therefore likely underestimate the strength of individual connections.

To get a more accurate account of how often an axon establishes multiple synapses on its postsynaptic partners, we proofread the axon and postsynaptic partners of a layer 3 pyramidal neuron that had been identified by CREST as establishing at least 19 synapses on one nearby interneuron. Most of its postsynaptic partners (387 of 397; 97.5%) received one (72%), two (16%), three (7%), or four (2%) synaptic contacts from this axon. These contacts were generally formed by relatively straight axonal branches appearing to be incidental to their juxtaposition with the dendrites that they innervated, which is consistent with Peters'

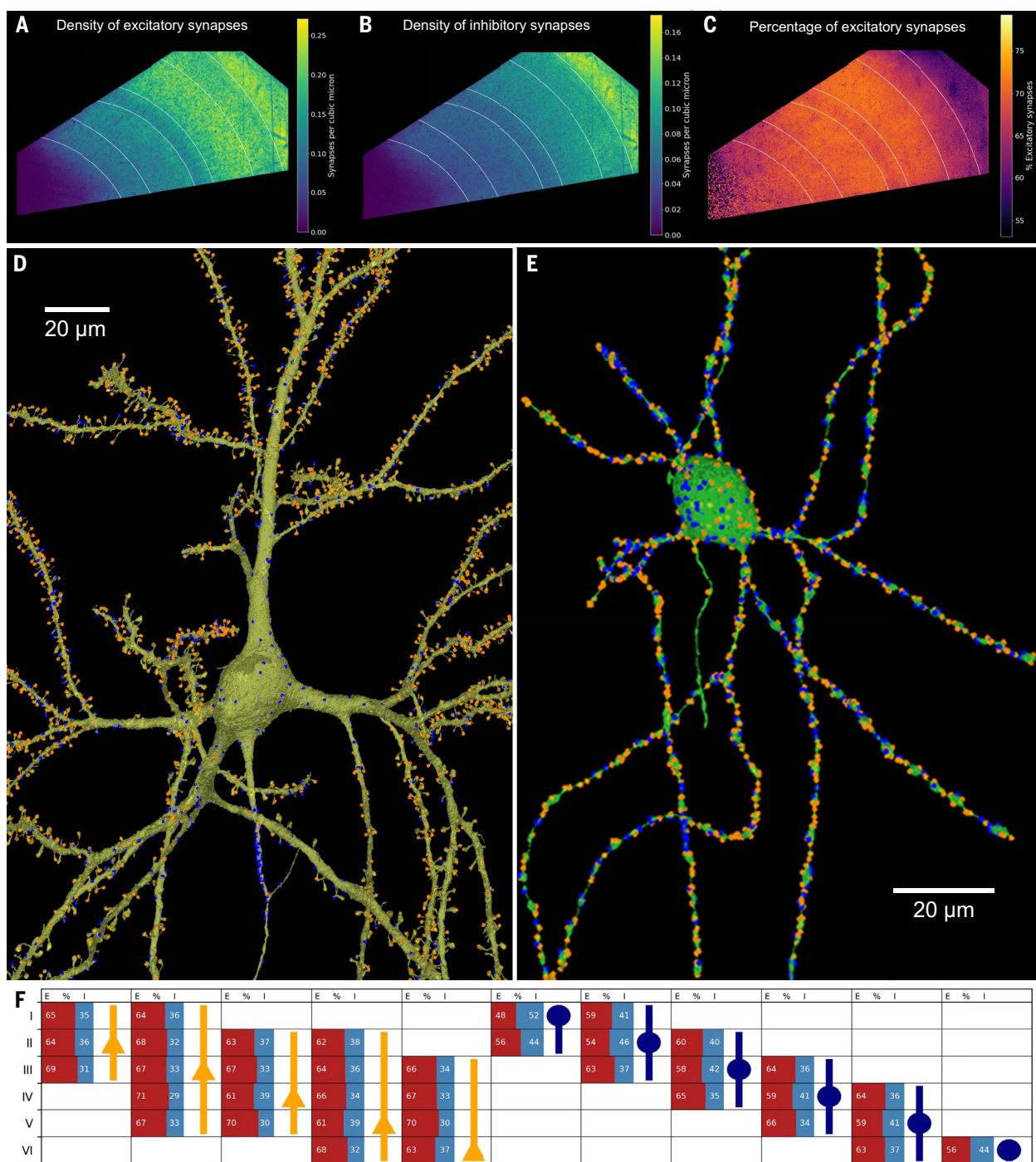


Fig. 5. Synapse distributions. (A) Volumetric density of excitatory (E) synapses. (B) Volumetric density of inhibitory (I) synapses. (C) Percentage of excitatory synapses in different layers (calculated as $E/(E + I) * 100\%$). Lowest values are purple; highest values are yellow. (D) Representative pyramidal neuron, with excitatory (orange) and inhibitory (blue) synapses shown. (E) Representative interneuron. (F) Plot of percentages of excitatory

(red bars) and inhibitory (blue bars) synaptic inputs in different cortical layers (row names) to different neuron types. Orange triangles represent pyramidal neurons, and blue circles represent interneurons; their row locations indicate the cortical layer location of their cell bodies. Data are shown for each cortical layer in which at least 100 cells of that type receive synaptic inputs.

rule (57). By contrast, at eight sites where the axon crossed dendrites of a nearby inhibitory interneuron, it established a spatially restricted cluster of synapses at each site, giving rise to a total of 53 synapses between this pair of cells

(Fig. 7E). This excitatory axon also strongly innervated four other inhibitory neurons in its vicinity. To assess whether this pyramidal neuron was exceptional, we also reconstructed the axon of a nearby layer 3 pyramidal neuron

and its 251 postsynaptic partners. It was found to have three strong connections (more than seven synapses), including 30 synapses with an inhibitory partner and 13 synapses with an excitatory partner (see table S9 for all data).

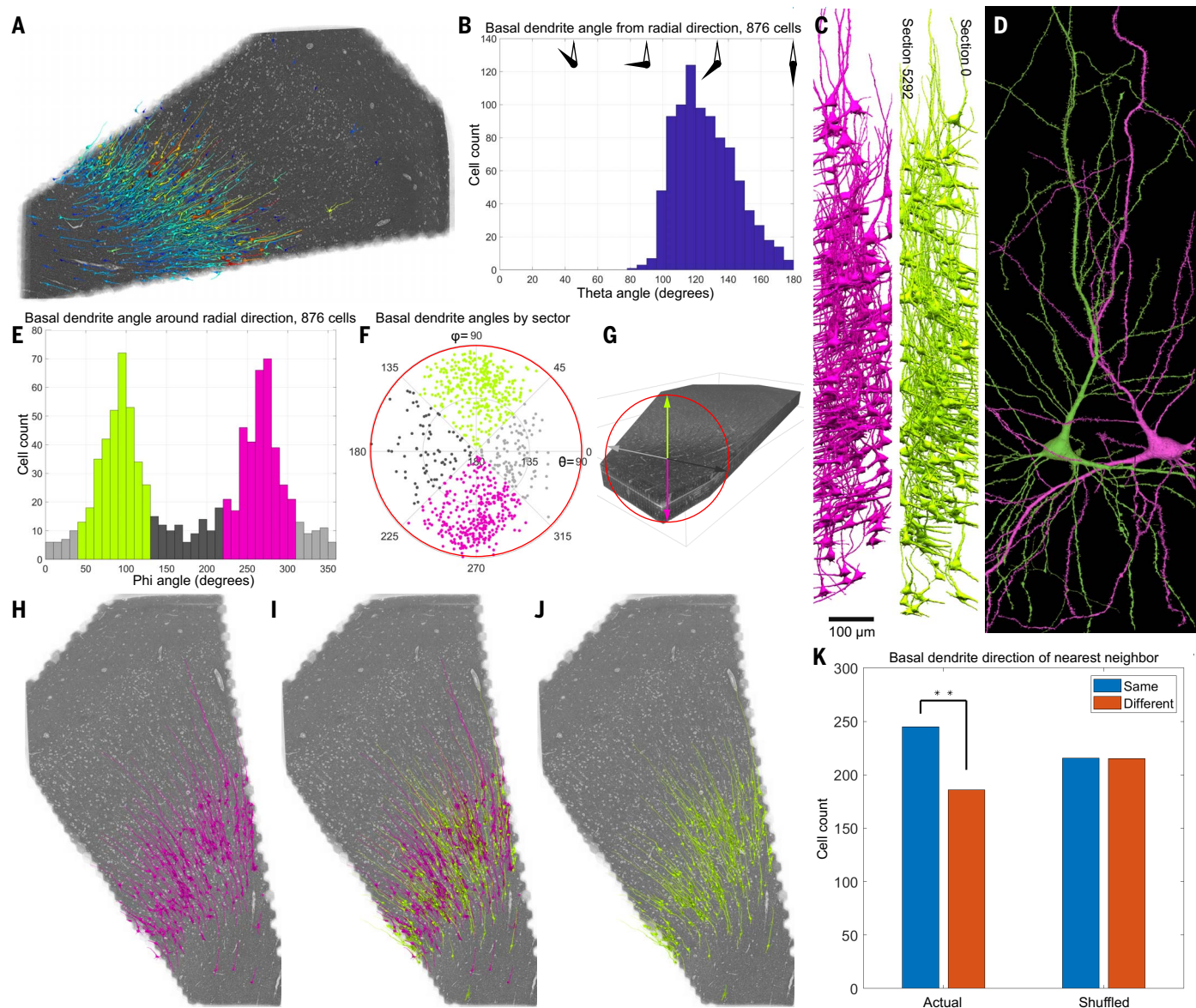


Fig. 6. Two mirror symmetrical subgroups of deep layer triangular neurons.

(A) Location of neurons with both one large apical and one large basal dendrite. Color represents cell soma size, as in Fig. 4A. (B) Distribution of directions of the basal dendrites of triangular neurons, where the direction is the angle between the radial direction and the basal dendrite direction. (C) Side view of the neurons with apical dendrites pointing either forward in the z-stack (magenta) or in the reverse direction (light green). (D) Example of two triangular neurons with basal dendrites pointing in opposite directions showing the mirror symmetry of these two subgroups. (E) Histogram of basal dendrite angles around the

radial direction. (F) Polar plot of the data in (B) and (E). Light green indicates the 339 triangular cells with basal dendrites pointing toward section 0; magenta indicates the 347 triangular cells with basal dendrites pointing toward section 5292; light and dark gray indicate the 106 and 80 triangular cells, respectively, with basal dendrites pointing sideways in the cutting plane. (G) Explanation of the directional color coding in this figure. (H to J) Anatomical clustering among members of the two subgroups. (K) Bar graph comparing the basal dendrite direction of each cell with its nearest neighbor in the actual data (left) and control with dendrite directions shuffled (right).

Many of these strong connections shared a common morphological configuration. In some cases, the axon co-fasciculated with the dendrite to remain in close contact for tens of micrometers, allowing it to establish many en passant synapses with the same target cell (as shown in Fig. 7C). More commonly, however, the axon did not appear to have a special affinity for growing along the dendrite and instead approached the dendrite, as was

typical of axons that made one-synapse connections, by forming a synapse at the site of intersection without deviating its trajectory before or after the synapse. In addition to a synapse at the closest point of intersection, these axons sent terminal branches to the same target cell, usually on both sides of the intersection, suggesting that the axon may have sprouted “up” to establish synapses on the dendrite and sprouted its terminal branches

“down” to establish additional synapses with the same target cell on the other side (Fig. 7, A and B).

This motif is suggestive of purpose, meaning that some pre- or postsynaptic pairs had a reason to be far more strongly connected than was typical. The alternative possibility is that given the thousands of axonal inputs to each of thousands of target cells, outlier results are simply part of the long tail of a distribution.

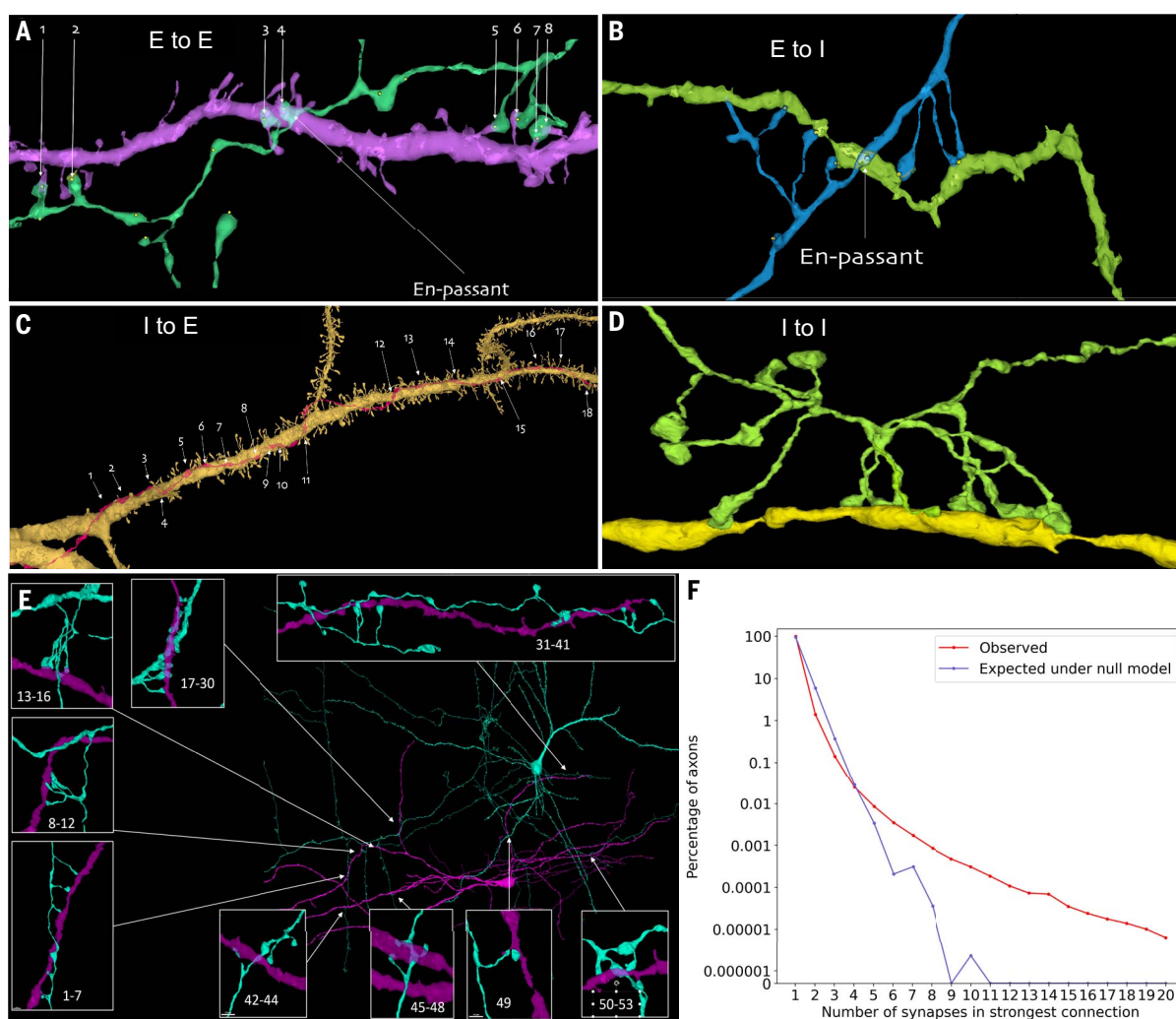


Fig. 7. Unusually powerful synaptic connections. (A) An excitatory axon (green) forms eight synapses onto a spiny dendrite of an excitatory neuron (purple). One synapse is en passant and the rest appear to require directed growth of the axon to contact the same dendrite. (B) An excitatory axon (blue) forms eight synapses onto a smooth dendrite of an inhibitory neuron (green), again, with one en passant connection and the rest apparently requiring directed growth. (C) An inhibitory axon (red) forming 18 synapses on the apical dendrite

of a spiny pyramidal excitatory neuron (yellow). (D) An inhibitory axon (green) forming nine synapses onto the smooth dendrite (yellow) of another inhibitory neuron. (E) A total of 53 synaptic connections from a proofread layer 3 pyramidal neuron onto a nearby inhibitory interneuron. (F) Plot comparing the observed (red line) and expected (blue line) percentage of axons making their strongest connection of between one and 20 synapses onto individual postsynaptic partners. The percentage is expressed on a log scale.

We therefore sought a conservative null model to simulate the number of axons with powerful connections if the connections were stochastically formed, based on the actual trajectories of axons and dendrites and the observed properties of axonal branches. The model allowed every simulated axon to form the same number of synapses that it did in the actual data, but now on any of the dendritic branches that came within its vicinity to match the reach of the actual axons (see the materials and methods). We were interested to see how often an axon would establish multiple synapses with a single target cell. The results indicate that this random model of synaptic partnering (Fig. 7F, blue line) is inconsistent with the incidence of strongly

paired neurons (Fig. 7F, red line) that we found in H01 ($P < 10^{-10}$, $n = 79,827,631$ axons analyzed). This tendency for axons to establish more synapses with certain target cells than would be expected by chance was found to be about the same when we analyzed just inhibitory or just excitatory axons (fig. S9). Thus, among a large number of exceedingly weak incidental connections, human cerebral cortex neurons appear to be innervated by a small subset of excitatory and inhibitory inputs that purposefully establish more powerful connections.

Discussion

The central tenet of connectomics is capturing both big and small scales by reconstructing

individual synaptic connections in volumes large enough to encompass neural circuits (58). Our aim in this work was to create a resource that allows the study of the structure of human six-layered cerebral cortex at nanometer-scale resolution within an approximately millimeter-scale volume. We chose a slab that extended from layer 1 to white matter (~3 mm) oriented along the plane of apical dendrites and principal axons with sufficient depth (170 μ m) to allow the tracing of axons across multiple cortical layers. The nanometer scale is required to identify individual synapses and to distinguish tightly packed axonal and dendritic processes from one another (59). We acquired trillions of voxels, and thus more than a petabyte of digital image data. This amount of data allows

for the visualization of the same volume of brain tissue at the supracellular, cellular, and subcellular levels and for studying the relationships between and among large numbers of annotated neurons, synapses, glia, and blood vessels. Perhaps most importantly, the resource presented here provides the opportunity to study the complicated synaptic relationships between many neurons in a slab of human association cerebral cortex.

To aid further study, we provide here several software tools. Neuroglancer is a browser-based tool that can be used to explore the H01 dataset visually, including the EM ultrastructure, the segmentations, and synaptic and cell type annotations. CREST, a tool that builds on Neuroglancer, enables the exploration of the synaptic pathways converging on or diverging from any neuron in the volume. CAVE also builds on Neuroglancer to provide community-based online proofreading of this multibeam dataset. Finally, VAST allows users to export, annotate, and measure any features in the dataset by skeletonization or voxel painting.

Using these tools in the H01 sample, we uncovered some interesting phenomena. In addition to several oddities (fig. S2), we found a morphological distinction between compass cells in layer 6 with basal dendrites that oriented in two preferred directions. We also found neurons that generated 50 or more synapses on individual postsynaptic partners. Other previously undescribed features might be found upon further analysis of this dataset.

Studying human brain samples has special challenges. Although tissue fixed after a short postmortem delay can be of sufficient quality to allow the identification of synapses (60), membranous structures containing no cytoplasm are sometimes observed, which are not seen in rapidly preserved samples. Fortunately, the histological quality of the H01 brain sample in terms of visualizing neurons, glia, and their organelles was equivalent to the rodent perfused cardiac samples used in the past (23, 25, 55). Because there were few membrane breaks, the data could be reconstructed both manually and with machine learning. This strongly suggests that rapid immersion of fresh tissue in fixative is a viable alternative to perfusion and should be especially useful in human connectomics studies going forward (61). More problematic is that fresh samples from healthy individuals are unlikely to ever be available through this neurosurgical route. Although this individual's temporal lobe did not show substantial pathological changes by light microscopy, as stated in the neuropathological report, it is possible that long-term epilepsy, or its treatment with pharmacological agents, had some more subtle effects on the connectivity or structure of the cortical tissue. There were some oddities identified in this tissue, including a number of extremely

large spines, axon varicosities filled with unusual material, and a small number of axons that formed extensive whorls (fig. S2). At present, we are unable to determine whether these resulted from a pathological process or if they are simply rare. Comparing samples obtained from individuals with different underlying disorders will allow for a better understanding of the phenomena seen here.

Another challenge with studying human brain tissue from association cortex is that its circuits are likely established, at least in part, as a consequence of experience, raising the question of how similar one person's association cortex will be to another's. Although atlases describing intersubject variability of human cortex exist for the micro- and macroscopic scales (62), a lack of human datasets at the nanometer scale means that intersubject variability of human cortical microcircuits is currently not known. Between individual *Caenorhabditis elegans* nematodes with identical genomes, although the majority of connections were stereotyped, 40% of the neuron-to-neuron connectivity differed between individuals (19). Given the far greater variability in human experience, behavior, and genetics, and the fact that humans and other vertebrates have pools of identified neuron classes (63) rather than individual identified neuron types, it may be more challenging to compare neural circuits between human brains. This challenge also presents an opportunity to uncover the physical instantiation of learned information. Even if the circuits differ in their particulars, it is possible that a metalogic for memory can be found by looking at enough data in the future field of "engramics" (64, 65).

Without question, approaches to uncovering the meaning of neural circuit connectivity data are in their infancy, but this petascale dataset is a start.

Methods summary

Tissue resected from the anterior middle temporal gyrus underwent rapid immersion fixation and staining with osmium and other heavy metals (27). The sample was then embedded in resin, and 5019 sections were collected at an average thickness of 33.9 nm using an automatic tape-collecting ultramicrotome (ATUM) (28) for a total sample thickness of 0.170 mm. Sections were imaged using a multibeam scanning EM at $4 \times 4 \text{ nm}^2$ resolution (Fig. 1A), giving a total imaged volume of 1.05 mm^3 after correcting for a compression of 28% in the cutting direction, and a raw data size of up to 350 gigabytes per section, or 1.8 petabytes in total.

From a total of 247 million tiles, 196 million image tiles were stitched together and coarsely aligned by using microscope stage coordinates and image features to relax an elastic triangular mesh of each tile and each section (Fig. 1B, left). A fine-scale refining alignment based on optical flow between neighboring sections re-

moved remaining drift and jitter from the unified ~1.4 petabyte image volume (Fig. 1B, center and right).

A multiresolution FFN was used to segment the image data (29), producing base segments (Fig. 2A) that were then agglomerated using FFN resegmentation to produce more complete reconstructed cells and processes (Fig. 2B). Because occasional agglomeration errors produced mergers between nearby objects (Fig. 2C, left), we skeletonized the segmentation and classified skeleton nodes within each cell as axon, dendrite, astrocyte, soma, cilium, or AIS (Fig. 2C, center), allowing an automated cut to be made at the site of merge errors (Fig. 2C, right).

To identify synaptic sites, we trained a classifier based on a U-Net architecture to label three classes: background, presynaptic, and postsynaptic (Fig. 2D). We trained a two-class ResNet-50 classifier to classify each identified synapse as excitatory or inhibitory based on its EM appearance, postsynaptic structure type, and presynaptic neuron type, if known.

REFERENCES AND NOTES

1. D. S. Tuch et al., High angular resolution diffusion imaging reveals intravoxel white matter fiber heterogeneity. *Magn. Reson. Med.* **48**, 577–582 (2002). doi: [10.1002/mrm.10268](https://doi.org/10.1002/mrm.10268); pmid: [12353272](https://pubmed.ncbi.nlm.nih.gov/12353272/)
2. B. L. Edlow et al., 7 Tesla MRI of the ex vivo human brain at 100 micron resolution. *Sci. Data* **6**, 244 (2019). doi: [10.1038/s41597-019-0254-8](https://doi.org/10.1038/s41597-019-0254-8); pmid: [31666530](https://pubmed.ncbi.nlm.nih.gov/31666530/)
3. J. Bijsterbosch et al., Challenges and future directions for representations of functional brain organization. *Nat. Neurosci.* **23**, 1484–1495 (2020). doi: [10.1038/s41593-020-00726-z](https://doi.org/10.1038/s41593-020-00726-z); pmid: [32106677](https://pubmed.ncbi.nlm.nih.gov/32106677/)
4. A. Yendiki et al., Post mortem mapping of connectional anatomy for the validation of diffusion MRI. *Neuroimage* **256**, 119146 (2022). doi: [10.1016/j.neuroimage.2022.119146](https://doi.org/10.1016/j.neuroimage.2022.119146); pmid: [35346838](https://pubmed.ncbi.nlm.nih.gov/35346838/)
5. M. Axer, K. Amunts, Scale matters: The nested human connectome. *Science* **378**, 500–504 (2022). doi: [10.1126/science.abq2599](https://doi.org/10.1126/science.abq2599); pmid: [36378967](https://pubmed.ncbi.nlm.nih.gov/36378967/)
6. Y. Meirovitch et al., Neuromuscular connectomes across development reveal synaptic ordering rules, *bioRxiv* (2021). <https://doi.org/10.1101/2021.09.20.460480>
7. J. Lu, J. C. Tapia, O. L. White, J. W. Lichtman, The interscutular muscle connectome. *PLOS Biol.* **7**, e32 (2009). pmid: [19209956](https://pubmed.ncbi.nlm.nih.gov/19209956/)
8. M. Lakadamyali, H. Babcock, M. Bates, X. Zhuang, J. Lichtman, 3D multicolor super-resolution imaging offers improved accuracy in neuron tracing. *PLOS ONE* **7**, e30826 (2012). doi: [10.1371/journal.pone.0030826](https://doi.org/10.1371/journal.pone.0030826); pmid: [2292051](https://pubmed.ncbi.nlm.nih.gov/2292051/)
9. B. M. White, P. Kumar, A. N. Conwell, K. Wu, J. M. Baskin, Lipid expansion microscopy. *J. Am. Chem. Soc.* **144**, 18212–18217 (2022). doi: [10.1021/jacs.2c03743](https://doi.org/10.1021/jacs.2c03743); pmid: [36190998](https://pubmed.ncbi.nlm.nih.gov/36190998/)
10. O. M'Saad et al., All-optical visualization of specific molecules in the ultrastructural context of brain tissue, *bioRxiv* 486901 [Preprint] (2022); <https://doi.org/10.1101/2022.04.04.486901>.
11. A. T. Kuan et al., Dense neuronal reconstruction through X-ray holographic nano-tomography. *Nat. Neurosci.* **23**, 1637–1643 (2020). doi: [10.1038/s41593-020-0704-9](https://doi.org/10.1038/s41593-020-0704-9); pmid: [32929244](https://pubmed.ncbi.nlm.nih.gov/32929244/)
12. H. Wang, C. Magnain, S. Sakadžić, B. Fischl, D. A. Boas, Characterizing the optical properties of human brain tissue with high numerical aperture optical coherence tomography. *Biomed. Opt. Express* **8**, 5617–5636 (2017). doi: [10.1364/BOE.8.005617](https://doi.org/10.1364/BOE.8.005617); pmid: [29296492](https://pubmed.ncbi.nlm.nih.gov/29296492/)
13. P. W. Tillberg et al., Protein-retention expansion microscopy of cells and tissues labeled using standard fluorescent proteins and antibodies. *Nat. Biotechnol.* **34**, 987–992 (2016). doi: [10.1038/nbt.3625](https://doi.org/10.1038/nbt.3625); pmid: [27376584](https://pubmed.ncbi.nlm.nih.gov/27376584/)
14. Y. M. Sigal, C. M. Speer, H. P. Babcock, X. Zhuang, Mapping synaptic input fields of neurons with super-resolution imaging. *Cell* **163**, 493–505 (2015). doi: [10.1016/j.cell.2015.08.033](https://doi.org/10.1016/j.cell.2015.08.033); pmid: [26435106](https://pubmed.ncbi.nlm.nih.gov/26435106/)

15. N. Aleksejenko, J. P. Heller, Super-resolution imaging to reveal the nanostructure of tripartite synapses. *Neuronal Signal.* **5**, NS20210003 (2021). doi: [10.1042/NS20210003](https://doi.org/10.1042/NS20210003); pmid: [34737894](https://pubmed.ncbi.nlm.nih.gov/34737894/)

16. J. M. Michalska et al., Imaging brain tissue architecture across millimeter to nanometer scales. *Nat. Biotechnol.* (2023). doi: [10.1038/s41587-023-01911-8](https://doi.org/10.1038/s41587-023-01911-8); pmid: [37653226](https://pubmed.ncbi.nlm.nih.gov/37653226/)

17. L. K. Scheffer et al., A connectome and analysis of the adult *Drosophila* central brain. *eLife* **9**, e57443 (2020). doi: [10.7554/elife.57443](https://doi.org/10.7554/elife.57443); pmid: [32880371](https://pubmed.ncbi.nlm.nih.gov/32880371/)

18. Z. Zheng et al., A complete electron microscopy volume of the brain of adult *Drosophila melanogaster*. *Cell* **174**, 730–743.e22 (2018). doi: [10.1016/j.cell.2018.06.019](https://doi.org/10.1016/j.cell.2018.06.019); pmid: [30033368](https://pubmed.ncbi.nlm.nih.gov/30033368/)

19. D. Witvliet et al., Connectomes across development reveal principles of brain maturation. *Nature* **596**, 257–261 (2021). doi: [10.1038/s41586-021-03778-8](https://doi.org/10.1038/s41586-021-03778-8); pmid: [34349261](https://pubmed.ncbi.nlm.nih.gov/34349261/)

20. A. Motta et al., Dense connectomic reconstruction in layer 4 of the somatosensory cortex. *Science* **366**, eaay3134 (2019). doi: [10.1126/science.aaay3134](https://doi.org/10.1126/science.aaay3134); pmid: [31649140](https://pubmed.ncbi.nlm.nih.gov/31649140/)

21. A. Gour et al., Postnatal connectomic development of inhibition in mouse barrel cortex. *Science* **371**, eabb4534 (2021). doi: [10.1126/science.abb4534](https://doi.org/10.1126/science.abb4534); pmid: [33273061](https://pubmed.ncbi.nlm.nih.gov/33273061/)

22. S. Loomba et al., Connectomic comparison of mouse and human cortex. *Science* **377**, eab0924 (2022). doi: [10.1126/science.abo0924](https://doi.org/10.1126/science.abo0924); pmid: [35737810](https://pubmed.ncbi.nlm.nih.gov/35737810/)

23. D. D. Bock et al., Network anatomy and in vivo physiology of visual cortical neurons. *Nature* **471**, 177–182 (2011). doi: [10.1038/nature09802](https://doi.org/10.1038/nature09802); pmid: [21390124](https://pubmed.ncbi.nlm.nih.gov/21390124/)

24. W.-C. A. Lee et al., Anatomy and function of an excitatory network in the visual cortex. *Nature* **532**, 370–374 (2016). doi: [10.1038/nature1792](https://doi.org/10.1038/nature1792); pmid: [27018655](https://pubmed.ncbi.nlm.nih.gov/27018655/)

25. N. Kasthuri et al., Saturated reconstruction of a volume of neocortex. *Cell* **162**, 648–661 (2015). doi: [10.1016/j.cell.2015.06.054](https://doi.org/10.1016/j.cell.2015.06.054); pmid: [26232230](https://pubmed.ncbi.nlm.nih.gov/26232230/)

26. M. Thom et al., Temporal lobe sclerosis associated with hippocampal sclerosis in temporal lobe epilepsy: Neuropathological features. *J. Neuropathol. Exp. Neurol.* **68**, 928–938 (2009). doi: [10.1097/NEN.0b013e3181b05d67](https://doi.org/10.1097/NEN.0b013e3181b05d67); pmid: [19606061](https://pubmed.ncbi.nlm.nih.gov/19606061/)

27. J. C. Tapia et al., High-contrast en bloc staining of neuronal tissue for field emission scanning electron microscopy. *Nat. Protoc.* **7**, 193–206 (2012). doi: [10.1038/nprot.2011.439](https://doi.org/10.1038/nprot.2011.439); pmid: [22240582](https://pubmed.ncbi.nlm.nih.gov/22240582/)

28. K. J. Hayworth et al., Imaging ATUM ultrathin section libraries with WaferMapper: A multi-scale approach to EM reconstruction of neural circuits. *Front. Neural Circuits* **8**, 68 (2014). doi: [10.3389/fncir.2014.00068](https://doi.org/10.3389/fncir.2014.00068); pmid: [25018701](https://pubmed.ncbi.nlm.nih.gov/25018701/)

29. M. Januszewski et al., High-precision automated reconstruction of neurons with flood-filling networks. *Nat. Methods* **15**, 605–610 (2018). doi: [10.1038/s41592-018-0049-4](https://doi.org/10.1038/s41592-018-0049-4); pmid: [30013046](https://pubmed.ncbi.nlm.nih.gov/30013046/)

30. S. Dorkenwald et al., CAVE: Connectome Annotation Versioning Engine. bioRxiv 550598 [Preprint] (2023); <https://doi.org/10.1101/2023.07.26.550598>.

31. D. R. Berger, H. S. Seung, J. W. Lichtman, VAST (Volume Annotation and Segmentation Tool): Efficient manual and semi-automatic labeling of large 3D image stacks. *Front. Neural Circuits* **12**, 88 (2018). doi: [10.3389/fncir.2018.00088](https://doi.org/10.3389/fncir.2018.00088); pmid: [30386216](https://pubmed.ncbi.nlm.nih.gov/30386216/)

32. A. Shapson-Coe, Video demonstration of the use of the Neuroglancer interface to explore the H01 dataset. Zenodo (2024); <https://zenodo.org/doi/10.5281/zenodo.10875297>.

33. J. DeFelipe, L. Alonso-Nanclares, J. I. Arellano, Microstructure of the neocortex: Comparative aspects. *J. Neurocytol.* **31**, 299–316 (2002). doi: [10.1023/A:1024130211265](https://doi.org/10.1023/A:1024130211265); pmid: [12815249](https://pubmed.ncbi.nlm.nih.gov/12815249/)

34. T. C. Murakami et al., A three-dimensional single-cell-resolution whole-brain atlas using CUBIC-X expansion microscopy and tissue clearing. *Nat. Neurosci.* **21**, 625–637 (2018). doi: [10.1038/s41593-018-0109-1](https://doi.org/10.1038/s41593-018-0109-1); pmid: [29507408](https://pubmed.ncbi.nlm.nih.gov/29507408/)

35. D. Keller, C. Erb, H. Markram, Cell densities in the mouse brain: A systematic review. *Front. Neuroanat.* **12**, 83 (2018). doi: [10.3389/fnana.2018.00083](https://doi.org/10.3389/fnana.2018.00083); pmid: [30405363](https://pubmed.ncbi.nlm.nih.gov/30405363/)

36. T. M. Consortium et al., Functional connectomics spanning multiple areas of mouse visual cortex. bioRxiv 454025 [Preprint] (2023); <https://doi.org/10.1101/2021.07.28.454025>.

37. G. Rajkowska, L. D. Selenton, P. S. Goldman-Rakic, Neuronal and glial somal size in the prefrontal cortex: A postmortem morphometric study of schizophrenia and Huntington disease. *Arch. Gen. Psychiatry* **55**, 215–224 (1998). doi: [10.1001/archpsyc.55.3.215](https://doi.org/10.1001/archpsyc.55.3.215); pmid: [9510215](https://pubmed.ncbi.nlm.nih.gov/9510215/)

38. E. A. Bushong, M. E. Martone, Y. Z. Jones, M. H. Ellisman, Protoplasmic astrocytes in CA1 stratum radiatum occupy separate anatomical domains. *J. Neurosci.* **22**, 183–192 (2002). doi: [10.1523/JNEUROSCI.22-01-00183.2002](https://doi.org/10.1523/JNEUROSCI.22-01-00183.2002); pmid: [11756501](https://pubmed.ncbi.nlm.nih.gov/11756501/)

39. K. Ogata, T. Kosaka, Structural and quantitative analysis of astrocytes in the mouse hippocampus. *Neuroscience* **113**, 221–233 (2002). doi: [10.1016/S0306-4522\(02\)00041-6](https://doi.org/10.1016/S0306-4522(02)00041-6); pmid: [12123700](https://pubmed.ncbi.nlm.nih.gov/12123700/)

40. M. M. Halassa, T. Fellin, H. Takano, J.-H. Dong, P. G. Haydon, Synaptic islands defined by the territory of a single astrocyte. *J. Neurosci.* **27**, 6473–6477 (2007). doi: [10.1523/JNEUROSCI.1419-07.2007](https://doi.org/10.1523/JNEUROSCI.1419-07.2007); pmid: [17567808](https://pubmed.ncbi.nlm.nih.gov/17567808/)

41. R. Fang et al., Conservation and divergence of cortical cell organization in human and mouse revealed by MERFISH. *Science* **377**, 56–62 (2022). doi: [10.1126/science.abm1741](https://doi.org/10.1126/science.abm1741); pmid: [3571910](https://pubmed.ncbi.nlm.nih.gov/3571910/)

42. S. Dorkenwald et al., Multi-layered maps of neuropil with segmentation-guided contrastive learning. *Nat. Methods* **20**, 2011–2020 (2023). doi: [10.1038/s41592-023-02059-8](https://doi.org/10.1038/s41592-023-02059-8); pmid: [37985712](https://pubmed.ncbi.nlm.nih.gov/37985712/)

43. J. M. Soares, P. Marques, V. Alves, N. Sousa, A hitchhiker's guide to diffusion tensor imaging. *Front. Neurosci.* **7**, 31 (2013). doi: [10.3389/fnins.2013.00031](https://doi.org/10.3389/fnins.2013.00031); pmid: [23486659](https://pubmed.ncbi.nlm.nih.gov/23486659/)

44. S. Y. Huang et al., Connectome 2.0: Developing the next-generation ultra-high gradient strength human MRI scanner for bridging studies of the micro-, meso- and macro-connectome. *NeuroImage* **243**, 118530 (2021). doi: [10.1016/j.neuroimage.2021.118530](https://doi.org/10.1016/j.neuroimage.2021.118530); pmid: [34464739](https://pubmed.ncbi.nlm.nih.gov/34464739/)

45. J. J. Harris, D. Attwell, The energetics of CNS white matter. *J. Neurosci.* **32**, 356–371 (2012). doi: [10.1523/JNEUROSCI.3430-11.2012](https://doi.org/10.1523/JNEUROSCI.3430-11.2012); pmid: [22219296](https://pubmed.ncbi.nlm.nih.gov/22219296/)

46. W. R. Brown, A Review of *String Vessels or Collapsed, Empty Basement Membrane Tubes* (IOS Press, 2010); <https://doi.org/10.3233/jad-2010-100219>.

47. L. Mendes-Jorge et al., Intercapillary bridging cells: Immunocytochemical characteristics of cells that connect blood vessels in the retina. *Exp. Eye Res.* **98**, 79–87 (2012). doi: [10.1016/j.exer.2012.03.010](https://doi.org/10.1016/j.exer.2012.03.010); pmid: [22484557](https://pubmed.ncbi.nlm.nih.gov/22484557/)

48. L. Alarcon-Martinez et al., Interpericyte tunnelling nanotubes regulate neuromuscular coupling. *Nature* **585**, 91–95 (2020). doi: [10.1038/s41586-020-2589-x](https://doi.org/10.1038/s41586-020-2589-x); pmid: [32788726](https://pubmed.ncbi.nlm.nih.gov/32788726/)

49. F. Briggs, Organizing principles of cortical layer 6. *Front. Neural Circuits* **4**, 3 (2010). pmid: [2019784](https://pubmed.ncbi.nlm.nih.gov/2019784/)

50. E. M. Callaway, Cell types and local circuits in primary visual cortex of the macaque monkey. *Vis. Neurosci.* **1**, 680–694 (2004).

51. S. Ramón y Cajal, *Histologie du système nerveux de l'homme et des vertébrés* (A. Maloine, 1909).

52. M. De Crinis, Über die Spezialzellen in der menschlichen Grosshirnrinde. *J. Psychol. Neurol.* **45**, 439–449 (1934).

53. H. Braak, *Architectonics of the Human Telencephalic Cortex* (Springer, 1980). doi: [10.1007/978-3-642-81522-5](https://doi.org/10.1007/978-3-642-81522-5)

54. A. Burkhalter, K. L. Bernardo, V. Charles, Development of local circuits in human visual cortex. *J. Neurosci.* **13**, 1916–1931 (1993). doi: [10.1523/JNEUROSCI.13-05-01916.1993](https://doi.org/10.1523/JNEUROSCI.13-05-01916.1993); pmid: [8478684](https://pubmed.ncbi.nlm.nih.gov/8478684/)

55. H. Schmidt et al., Axonal synapse sorting in medial entorhinal cortex. *Nature* **549**, 469–475 (2017). doi: [10.1038/nature24005](https://doi.org/10.1038/nature24005); pmid: [28959971](https://pubmed.ncbi.nlm.nih.gov/28959971/)

56. J. DeFelipe, S. H. Hendry, E. G. Jones, D. Schmechel, Variability in the terminations of GABAergic chandelier cell axons on initial segments of pyramidal cell axons in the monkey sensory-motor cortex. *J. Comp. Neurol.* **231**, 364–384 (1985). doi: [10.1002/cne.902310307](https://doi.org/10.1002/cne.902310307); pmid: [29819077](https://pubmed.ncbi.nlm.nih.gov/29819077/)

57. V. Braitenberg, A. Schüz, *Cortex: Statistics and Geometry of Neuronal Connectivity* (Springer, 2013).

58. J. W. Lichtman, W. Denk, The big and the small: Challenges of imaging the brain's circuits. *Science* **334**, 618–623 (2011). doi: [10.1126/science.1209168](https://doi.org/10.1126/science.1209168); pmid: [22053041](https://pubmed.ncbi.nlm.nih.gov/22053041/)

59. Y. Mishchenko, Automation of 3D reconstruction of neural tissue from large volume of conventional serial section transmission electron micrographs. *J. Neurosci. Methods* **176**, 276–289 (2009). doi: [10.1016/j.jneumeth.2008.09.006](https://doi.org/10.1016/j.jneumeth.2008.09.006); pmid: [18834903](https://pubmed.ncbi.nlm.nih.gov/18834903/)

60. N. Cano-Astorga, S. Plaza-Alonso, J. DeFelipe, L. Alonso-Nanclares, 3D synaptic organization of layer III of the human anterior cingulate and temporopolar cortex. *Cereb. Cortex* **33**, 9691–9708 (2023). doi: [10.1093/cercor/bhac232](https://doi.org/10.1093/cercor/bhac232); pmid: [37455478](https://pubmed.ncbi.nlm.nih.gov/37455478/)

61. N. Karlupia et al., Immersion fixation and staining of multicubic millimeter volumes for electron microscopy-based connectomics of human brain biopsies. *Biol. Psychiatry* **94**, 352–360 (2023). doi: [10.1016/j.biopsych.2023.01.025](https://doi.org/10.1016/j.biopsych.2023.01.025); pmid: [36740206](https://pubmed.ncbi.nlm.nih.gov/36740206/)

62. K. Amunts, H. Mohlberg, S. Bludau, K. Zilles, Julich-Brain: A 3D probabilistic atlas of the human brain's cytoarchitecture. *Science* **369**, 988–992 (2020). doi: [10.1126/science.abb4588](https://doi.org/10.1126/science.abb4588); pmid: [32732281](https://pubmed.ncbi.nlm.nih.gov/32732281/)

63. J. W. Lichtman, H. Colman, Synapse elimination and indelible memory. *Neuron* **25**, 269–278 (2000). doi: [10.1016/S0896-6273\(00\)80934-4](https://doi.org/10.1016/S0896-6273(00)80934-4); pmid: [10719884](https://pubmed.ncbi.nlm.nih.gov/10719884/)

64. H. S. Seung, Reading the book of memory: Sparse sampling versus dense mapping of connectomes. *Neuron* **62**, 17–29 (2009). doi: [10.1016/j.neuron.2009.03.020](https://doi.org/10.1016/j.neuron.2009.03.020); pmid: [19376064](https://pubmed.ncbi.nlm.nih.gov/19376064/)

65. J. L. Morgan, J. W. Lichtman, Why not connectomics? *Nat. Methods* **10**, 494–500 (2013). doi: [10.1038/nmeth.2480](https://doi.org/10.1038/nmeth.2480); pmid: [23722208](https://pubmed.ncbi.nlm.nih.gov/23722208/)

66. H. Li, M. Januszewski, V. Jain, P. H. Li, "Neuronal subcompartment classification and merge error correction" in *Medical Image Computing and Computer Assisted Intervention – MICCAI 2020: 23rd International Conference, Lima, Peru, October 4–8, 2020, Proceedings, Part V* (Springer, 2020), pp. 88–98.

67. S. Saalfeld, R. Fetter, A. Cardona, P. Tomancak, Elastic volume reconstruction from series of ultra-thin microscopy sections. *Nat. Methods* **9**, 717–720 (2012). doi: [10.1038/nmeth.2072](https://doi.org/10.1038/nmeth.2072); pmid: [22688414](https://pubmed.ncbi.nlm.nih.gov/22688414/)

68. Ö. Çiçek, A. Abdulkadir, S. S. Lienkamp, T. Brox, O. Ronneberger, "3D U-Net: Learning dense volumetric segmentation from sparse annotation" in S. Ourselin, L. Joskowicz, M. Sabuncu, G. Unal, W. Wells, Eds., *MICCAI 2016, Medical Image Computing and Computer-Assisted Intervention* (Springer, 2016), vol. 9901; https://doi.org/10.1007/978-3-319-46723-8_49.

69. D. R. Berger, H01 MATLAB analysis scripts. Zenodo (2024); [http://dx.doi.org/10.5281/zenodo.1057634](https://doi.org/10.5281/zenodo.1057634).

70. A. Shapson-Coe, L. Baley, H01 analysis scripts. Zenodo (2024); [http://dx.doi.org/10.5281/zenodo.10579637](https://doi.org/10.5281/zenodo.10579637).

71. Y. Wu, mSEM_workflow_manager, Zenodo (2024); [http://dx.doi.org/10.5281/zenodo.10576633](https://doi.org/10.5281/zenodo.10576633).

72. M. Januszewski, T. Blakley, J.-M. Lueckmann, SOFIMA: Scalable Optical Flow-Based Image Montaging and Alignment, Zenodo (2024); <https://doi.org/10.5281/zenodo.10534541>.

73. T. Blakley, P. H. Li, J.-M. Lueckmann, M. Januszewski, A. Immer, Google connectomics utilities, Zenodo (2024); <https://zenodo.org/records/10576375>.

74. A. Shapson-Coe, CREST: Connectome Reconstruction and Exploration Simple Tool, Zenodo (2024); [http://dx.doi.org/10.5281/zenodo.10580956](https://doi.org/10.5281/zenodo.10580956).

75. A. Shapson-Coe, A. Fitzmaurice, R. Kar, J. Wagner-Carena, D. Aley, J. Lau, H01 synapse ground truth, Zenodo (2024); [http://dx.doi.org/10.5281/zenodo.10864205](https://doi.org/10.5281/zenodo.10864205).

A.S.C., D.R.B., A.F., R.K., N.K. (production of ground truth for segmentation and agglomeration), P.H.L. (further correction of agglomeration), T.B. (synapse prediction and excitatory versus inhibitory classification), A.S.C., N.K., T.B., A.F., R.K., J.W.C., D.A., J.L., D.W., Z.L. (production of ground truth for synapse prediction and excitatory versus inhibitory classification), P.H.L. (skeletonization and subcompartment classification), P.H.L., A.S.C., A.F., R.K. (production of ground truth for skeletonization and subcompartment classification), S.D. (production of embeddings), E.S., D.R.B. (manual annotation and skeletonization of blood vessel cells), N.K. (manual reconstruction of whorled axons and identification of anomalous objects), D.R.B. (manual cell soma painting and classification); Methodology: A.Po. (development of alignment method), M.J. (development of fine-scale alignment with optical flow method); Project administration: J.W.L., V.J.; Software: J.M.S. (development of Neuroglancer software), L.L. (development and support of API), J.M.S., J.T., F.C., S.D. (development of CAVE software for use with H01 dataset), Y.W. (development of image quality assessment tools), A.S.C. (development of CREST program), D.R.B. (extension of VAST to access Google-hosted datasets); Supervision: J.W.L., V.J.; Validation: A.S.C., B.F., H.W., J.W.C., D.A., D.R.B., J.L., L.B. (proofreading of neurons), M.J., A.S.C., D.R.B. (measurement of segmentation split and merge error rates), T.B., D.R.B., A.S.C. (measurement of synapse prediction accuracy);

Visualization: D.R.B. (rendering of cells in Figs. 3, 4, 6, and 7E and the print summary figure), J.W.L. (rendering of neurons in Fig. 7, A to E); A.S.C. (Fig. 5) Writing – original draft: J.W.L., A.S.C., M.J., A.Po., D.R.B., T.B., P.H.L., V.J.; Writing – review & editing: J.W.L., A.S.C., D.R.B., V.J., M.J. **Competing interests:** The authors declare no competing interests. **Data and materials availability:** All data are available through the dedicated web page for this project: <http://h01-release.storage.googleapis.com/landing.html>, which also lists links to all code used for this project (<https://h01-release.storage.googleapis.com/code.html>). All previously published code used is cited in the text, including for flood-filling networks (29), subcompartment classification (66), EM image stitching and alignment (67), and volumetric segmentation from sparsely annotated data for synapse prediction (68). Code not previously published is archived in the Zenodo repository and cited in the text, including custom MATLAB code used for analysis (69), custom Python code used for analysis (70), code for automated EM data quality checks (71), code for fine-scale realignment (72), and various other code used in this project (73), as cited in the materials and methods section of the supplementary materials. Code and instructions for the CREST tool are available online (74). Ground truth data used to train networks to identify and classify synapses are available in Zenodo (75). Supporting files (in zip or original format) for individual scripts are included in

the repository or, if large, within a publicly available Google Cloud Storage repository, as indicated in the script in question. Several scripts use Google Cloud BigQuery databases, which are not publicly available and require a credentials file to access. However, the data contained within these databases is freely available for download from <http://h01-release.storage.googleapis.com/data.html>. Correspondence and requests for materials should be addressed to J.W.L. and V.J. **License information:** Copyright © 2024 the authors, some rights reserved; exclusive licensee American Association for the Advancement of Science. No claim to original US government works. <https://www.science.org/about/science-licenses-journal-article-reuse>

SUPPLEMENTARY MATERIALS

science.org/doi/10.1126/science.adk4858

Materials and Methods

Figs. S1 to S11

Tables S1 to S15

References (76–96)

MDAR Reproducibility Checklist

Movie S1

Submitted 10 September 2023; accepted 27 March 2024
10.1126/science.adk4858